Catalysis
Science &
Technology

ROYAL SOCIETY
OF CHEMISTRY

PAPER

View Article Online
View Journal | View Issue

Check for updates

Cite this: *Catal. Sci. Technol.*, 2024, **14**, 7134

Identification of Ni_3Fe alloy as a candidate catalyst for quinoline selective hydrogenation with computations†

Zhaochun He, ‡[abc] Yonghua Liu ‡[bc] and Tao Wang *[abc]

Received 8th September 2024,
Accepted 21st October 2024

DOI: 10.1039/d4cy01076k

rsc.li/catalysis

The 1,2,3,4-tetrahydroquinoline (py-THQL) is a crucial intermediate and fragment in chemical synthesis, but its production from quinoline (QL) selective hydrogenation in heterogeneous catalysis mainly relies on noble-metal-based catalysts. Therefore, the design of catalysts composed of earth-abundant elements for this reaction is meaningful. In this work, using density functional theory (DFT) calculations, we found the binding energy of QL to be a suitable descriptor to illustrate the general activity trend of metallic catalysts for QL hydrogenation. Among the screened bimetallic alloys composed of Fe, Co, Ni, and Cu, we computationally identified Ni_3Fe as a promising candidate catalyst with high stability, while our systematic mechanistic calculations showed the low energy barriers for each hydrogenation step. Our established DFT-based mean-field microkinetic model indicates a much higher turnover frequency for py-THQL production on the $Ni_3Fe(111)$ surface than on the experimentally reported high-performance $AuPd_3(111)$ surface. This work not only identified a valuable descriptor for the rational catalyst screening for the complex QL hydrogenation reaction but also theoretically predicted a cost-effective Ni_3Fe catalyst for the hydrogenation reaction.

1. Introduction

Nitrogen-containing compounds play pivotal roles in the pharmaceutical and agrochemical industries. Among them, 1,2,3,4-tetrahydroquinoline (py-THQL) and 5,6,7,8-tetrahydroquinoline (bz-THQL) are widely used as key intermediates and fragments in chemical synthesis.[1] In particular, the asymmetric structure and saturated N-heterocycle of py-THQL in various alkaloids and medicines enable its high chemical and biological activities against pathogenic bacteria and cancer cells.[2–4] Meanwhile, the py-THQL is also a crucial structure unit in dyes, working as an efficient sensitizer for dyes-sensitized solar cells (DSSCs).[5–7] Consequently, developing practical approaches for the efficient synthesis of py-THQL is meaningful for the aforementioned fields. Currently, there are three primary methods for py-THQL synthesis, including catalytic cyclization,[8] Beckman rearrangement,[9] and quinoline (QL) selective semi-hydrogenation.[4,10,11] Besides, the synthesis of py-THQL and derivatives through cross-coupling of quinoline with organic molecules could be achieved by using the electrochemical reductive method.[12,13] Among them, the selective semi-hydrogenation of QL using H_2 as the hydrogen source has the advantages of being a green process and having high atomic efficiency.[14] However, the selectivity control to avoid the formation of bz-THQL and decahydroquinoline (DHQL), as well as the harsh reaction conditions in this process, are the key challenges to be tackled,[15–17] which call for the design of high-performance catalysts.

The research on QL selective hydrogenation can be traced back to 1982, Fish *et al.*[10] identified Ru-based homogeneous catalysts to be active for this process, followed by the discoveries of Au,[18] Rh,[19] and Ir[20] complexes. Meanwhile, Pd, Pt, Ru, Co and Rh-based heterogeneous catalysts were also reported to exhibit outstanding performance in the QL hydrogenation reaction.[11,21–26] Apart from pure metals, alloying has been recently found to be an effective strategy to promote this reaction, and a group of alloys was reported to be promising, such as Au–Pd,[14] Pd–Ni,[27] Cu–Ru,[28] Ni–Ir,[29] Ni–Co,[30] Au_5Pt,[31] and $AuPd_3$.[32] Compared with the wide investigations experimentally, theoretical studies on the QL hydrogenation reaction have been relatively scarce due to the complex reaction mechanism. Xu and coworkers[33] studied QL hydrogenation to py-THQL on Ni-promoted MoS_2 with density functional theory

---

[a] *Division of Solar Energy Conversion and Catalysis at Westlake University, Zhejiang Baima Lake Laboratory Co., Ltd., Hangzhou 310000, Zhejiang, China. E-mail: twang@westlake.edu.cn*
[b] *Center of Artificial Photosynthesis for Solar Fuels and Department of Chemistry, School of Science and Research Center for Industries of the Future, Westlake University, 600 Dunyu Road, Hangzhou 310030, Zhejiang Province, China*
[c] *Institute of Natural Sciences, Westlake Institute for Advanced Study, 18 Shilongshan Road, Hangzhou 310024, Zhejiang Province, China*

† Electronic supplementary information (ESI) available. See DOI: **https://doi.org/10.1039/d4cy01076k**

‡ These authors contributed equally.

(DFT) calculations, where the reaction pathway followed the sequential hydrogenation of the N_4, C_3, C_2, and C_1 atoms on the N-heterocycle (atomic labels shown in Scheme 1). Similarly, Wang and coworkers[34] studied the QL hydrogenation mechanism on MoP(111) surface and found that the formation of py-THQL occurs *via* sequential hydrogenation of C_3, C_2, C_1, and N_4 atoms.

Indeed, the high complexity of the QL hydrogenation process (Fig. S1†) makes it computationally very expensive to conduct mechanism calculations on large numbers of catalysts and eventually hampers the rational design of earth-abundant catalysts for this reaction with computations. In this respect, the Sabatier principle capable of guiding the rational catalyst design for many reactions[35–41] will make efficient catalyst screening possible if adequate descriptors for QL hydrogenation can be identified.

In this work, we theoretically identified the binding energy of QL (E_{QL}) on metallic catalysts as an adequate descriptor for determining the activity of QL hydrogenation, where a volcano plot was established based on our previous joint experimental and theoretical studies of QL hydrogenation on AuPd-based alloys.[32] Then, we calculated the binding energy of QL on 18 bimetallic alloys composed of earth-abundant Fe, Co, Ni, and Cu elements. Among them, the Ni_3Fe alloy was theoretically predicted to be promising for QL hydrogenation. Our systematic DFT calculations and mean field microkinetic modeling (MKM) analysis showed that this Ni_3Fe catalyst exhibited higher TOF for py-THQL production than the $AuPd_3$ catalyst under the same reaction conditions. This work provides the theoretical feasibility of using NiFe-based alloy for QL selective hydrogenation.

2. Computational methods

All DFT calculations are implemented in the Vienna *ab initio* simulation package (VASP).[42] The BEEF-vdW functional[43] was used to describe the exchange-correlation contribution to the electronic energy due to its relatively high accuracy in describing the adsorption proprieties of adsorbates on transition metal surfaces. We employed the periodic surface slab model to simulate the adsorption and the hydrogenation process. The most stable (111) surface for FCC and (110) surface for BCC were chosen for the mechanistic study. The surface model is a 4-layered (4 × 4) supercell constrained bottom two layers and relaxed top two layers with a vacuum thickness of 15 Å to eliminate the interactions among the periodic surfaces. The cutoff energy was set to 400 eV to obtain accurate energy. All calculations were done when the force and energy difference were smaller than 0.05 eV $Å^{-1}$ and 10^{-4} eV, respectively. The binding energy of QL is defined as $E_{QL} = E_{(QL/surface)} - E_{(surface)} - E_{(QL)}$, where $E_{(QL/surface)}$, $E_{(surface)}$, and $E_{(QL)}$ are the total electronic energies of QL adsorbed on bimetallic catalysts surfaces, clean surfaces, and QL molecule in the gas phase, respectively. The transition states of each hydrogenation step are located by using the climbing image nudged elastic band (CINEB) method.[44] The Gibbs free energy barrier (G_a) is defined as the $G_a = G_{(TS)} - G_{(IS)}$, where $G_{(IS)}$, $G_{(TS)}$ are the free energies of initial states (IS) and transition state (TS) of each hydrogenation steps, respectively. All transition states are analyzed by frequency calculations with only one imaginary frequency. The thermodynamic corrections of adsorbates and gases are based on harmonic and ideal gas approximations as implemented in ASE.[45]

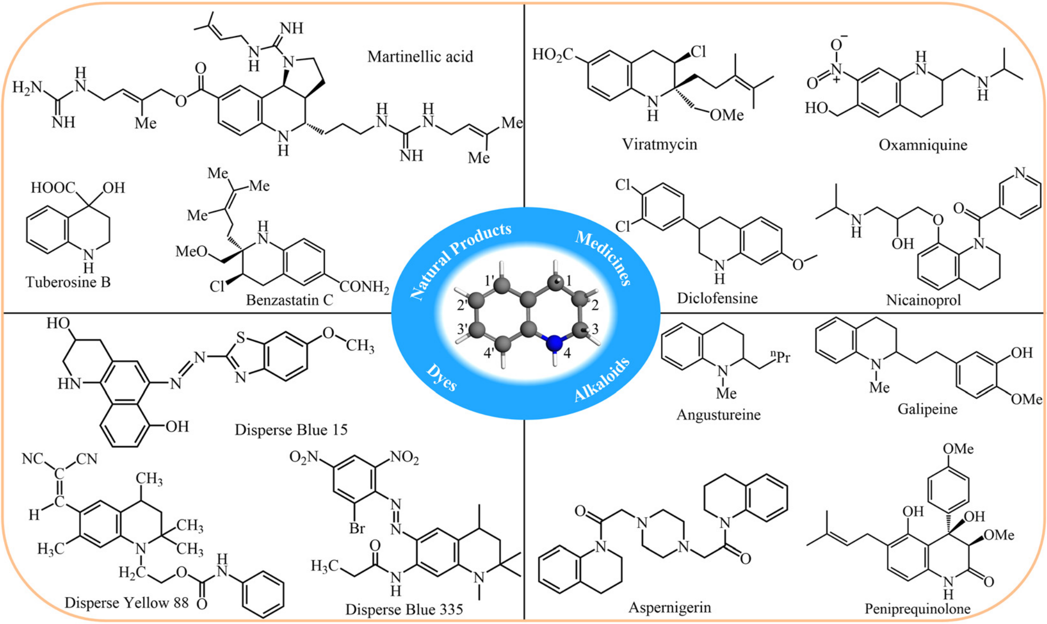

Scheme 1 Natural products, medicines, alkaloids, and dyes containing py-THQL framework, as well as the possible hydrogenation sites labeled as C_1, C_2, C_3, N_4, $C_{1'}$, $C_{2'}$, $C_{3'}$, $C_{4'}$.

3. Results and discussion

3.1. Sabatier principle for QL hydrogenation

To achieve an efficient screening of catalysts for QL hydrogenation, it is necessary to establish a rational activity trend for a group of well-studied catalysts, ideally from experimental results. Fortunately, we had the experimentally measured values of turnover frequencies (TOF) for QL hydrogenation on Au, $AuPd_3$, AuPd, Au_3Pd, and Pd in our previous joint experimental and theoretical studies.[32] Meanwhile, our mechanistic studies showed that the binding energy of QL on the metallic catalyst could work as a suitable descriptor to describe the general activity trend of the aforementioned AuPd-based catalysts. On this basis, the pure Pd catalyst with a too-strong binding of QL shows limited activity due to the surface poising, while the Au with a too-weak binding has difficulty activating reactants and eventually shows low activity. The AuPd-based alloys with moderate binding strength of QL show improved activity compared with the pure Au and Pd metals. Indeed, this follows the Sabatier principle well, which provides valuable guidance for our efficient screening of candidate catalysts for QL hydrogenation. As shown in Fig. S2,† we theoretically fitted the Sabatier volcano between E_{QL} and TOF of QL hydrogenation. Theoretically, the catalyst with an adequate E_{QL} may perform well for QL hydrogenation.

To design cost-effective catalysts for QL hydrogenation reaction, we focused on the alloys composed of earth-abundant Fe, Co, Ni, and Cu elements at three compositions (1 : 1, 1 : 2, and 1 : 3). Then, the close-packed surface of these 18 alloys were chosen as models to calculate the binding energy of QL. As shown in Fig. S3 and Table S2,† QL formed different adsorption configurations on these catalysts and had different binding energies. Then, we put these alloys on the Sabatier volcano in Fig. S2.† Among these 18 alloys, NiFe and CoNi-based alloys with proper compositions have the possibility to be located at the peak of the Sabatier volcano. To further evaluate the experimental feasibility, we calculated the formation energies of these 18 alloys, which were summarized in Table S2,† where the Ni_3Fe had the lowest formation energy and eventually a high stability. In this respect, we theoretically identified Ni_3Fe as a good candidate with high activity and stability for the QL hydrogenation reaction.

3.2. Quinoline hydrogenation mechanism on bimetallic Ni_3Fe catalyst

To further evaluate the performance of this theoretically predicted Ni_3Fe catalyst, we systematically calculated the detailed mechanisms of QL hydrogenation to py-THQL. Our calculated lattice parameters of bulk Ni_3Fe is $a = b = c = 3.6114$ Å, which agrees well with experimental values of $a = b = c = 3.5525$ Å.[46–48] This also indicates that our DFT calculations could reasonably describe the properties of Ni_3Fe alloy. As shown in Fig. 1, the hydrogenation process is very complex. For example, there are eight possibilities for the first hydrogenation step of QL on the $Ni_3Fe(111)$ surface to generate 1HQL, which directly determines the selectivity of QL hydrogenation. The eventual product formed in this process is determined by the relative ease with which H attacks a specific site of QL.

As shown in Fig. 1, the final states of 1HQL were named 1HQL-X, where the 1HQL-1, 1HQL-2, 1HQL-3, 1HQL-4, 1HQL-1′, 1HQL-2′, 1HQL-3′ and 1HQL-4′ correspond to the products of H attacking the C_1, C_2, C_3, N_4 atoms in N-heterocycle and $C_{1'}$, $C_{2'}$,

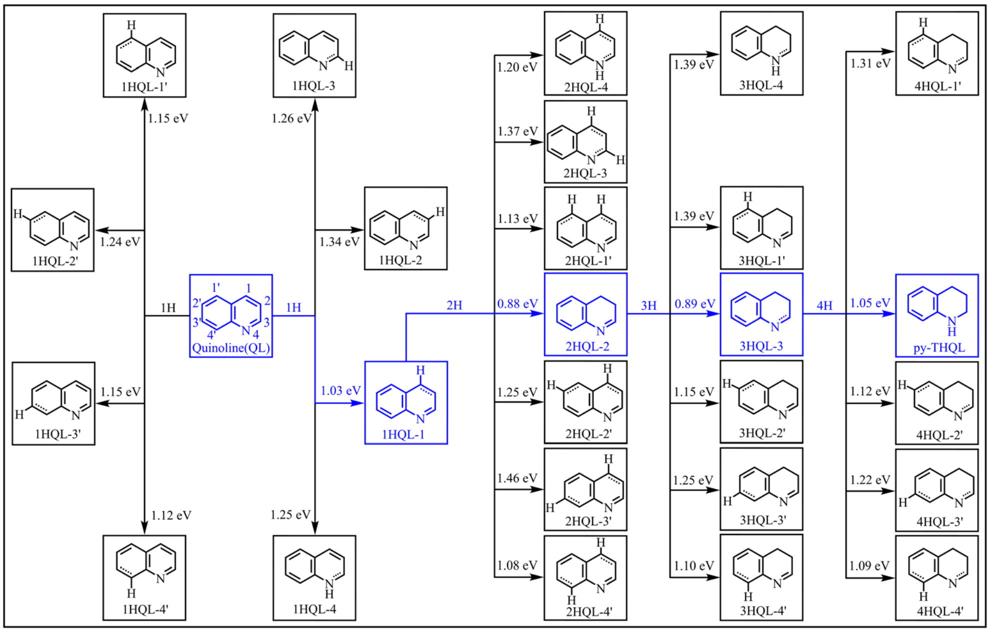

Fig. 1 The intermediates involved in the quinoline hydrogenation mechanism over the Ni_3Fe bimetallic catalyst and free energy barrier (G_a) at 353.15 K.

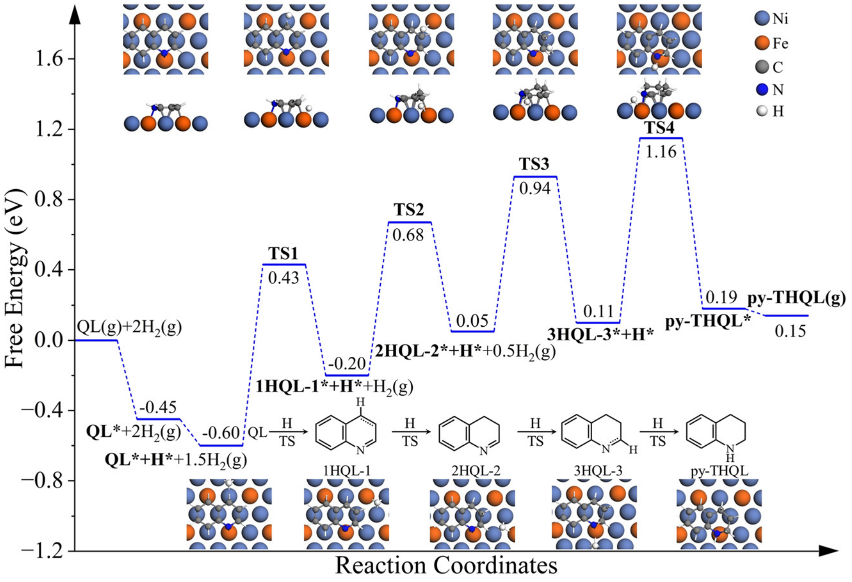

Fig. 2 The potential free energy diagram of QL hydrogenation on the bimetallic catalyst $Ni_3Fe(111)$ surface at 353.15 K with free energy corrections.

$C_{3'}$, $C_{4'}$ in benzene ring, respectively. Our calculations show that the first hydrogenation will take place at the C_1 site of the N-heterocycle due to the lower free energy barrier (1.03 eV) than the other possible pathways at 353.15 K. For the second hydrogenation step from 1HQL to 2HQL, we calculated the free energy barriers of seven possible hydrogenation pathways, where the second H could be added to C_2, C_3, N_4, $C_{1'}$, $C_{2'}$, $C_{3'}$, and $C_{4'}$. Our results show that the hydrogenation of the benzene ring is less favorable than the N-heterocycle ring. Among these processes, the hydrogenation of the C_2 site on the N-heterocycle ring has the lowest free energy barrier (0.88 eV). For the hydrogenation of 2HQL to 3HQL, six possible hydrogenation pathways were considered, where the hydrogenation of the C_3 site on the N-heterocycle ring had the lowest free energy barrier of 0.89 eV. The final hydrogenation step occurs at the N_4 site on the N-heterocycle ring with a free energy barrier of 1.05 eV. Noteworthy, the py-THQL product can not form chemical adsorption on the $Ni_3Fe(111)$ surface and is readily away from the surface (Fig. S4†), which hampers the further hydrogenation of the benzene ring to form the fully hydrogenated decahydroquinoline (DHQL).

3.3. Potential free energy diagram and MKM analysis

Based on the systematic calculations, we obtain the favorable reaction pathway of QL hydrogenation to py-THQL on the Ni_3Fe catalyst, which is the successive hydrogenation of the C_1, C_2, C_3, and N_4 sites of the N-heterocycle to generate intermediates 1HQL, 2HQL, 3HQL, and py-THQL. Then, we plotted the potential free energy diagram of QL hydrogenation on the $Ni_3Fe(111)$ surface at 353.15 K in Fig. 2. It shows that the maximum free energy barrier of the most favorable reaction pathway is 1.05 eV. We calculated the quinoline hydrogenation on $AuPd_3$ by repeating the reported pathway in our previous joint work using the same calculation parameters in this work. Indeed, these energy barriers are lower than those on our previously reported $AuPd_3$ catalyst[32] (Fig. S5†), where the free energy barrier for the rate-determining step on the $AuPd_3(111)$ surface is 1.37 eV. This indicates the potentially high activity of the predicted Ni_3Fe catalyst in the selective hydrogenation of QL to py-THQL.

To further evaluate the catalytic performance of the $Ni_3Fe(111)$ surface in QL hydrogenation, we established a mean-field microkinetic model to calculate the TOF of py-THQL production and more details could be found in ESI.† For convenience and clarity, we compared the activity of the $Ni_3Fe(111)$ surface with the $AuPd_3(111)$ surface. As shown in Fig. 3A and B, the TOF for py-THQL production on the $Ni_3Fe(111)$ surface is much higher than that on the $AuPd_3(111)$ surface at a wide range of reaction conditions. More specifically, at specific temperature of 500 K for quinoline hydrogenation in Fig. 3C, the theoretically calculated TOF of py-THQL production on Ni_3Fe (2.29×10^{-9} s^{-1}) is higher than $AuPd_3$ (7.5×10^{-12} s^{-1}) at 1 bar. Likewise, at a pressure of 100 bar in Fig. 3D, the theoretically calculated TOF is 1.86×10^{-4} s^{-1}, which is much higher than $AuPd_3$ (4.95×10^{-7} s^{-1}) at a temperature of 600 K. All these computational results indicate the high potential of this theoretically predicted Ni_3Fe catalyst in conducting effective QL hydrogenation.

4. Conclusions

In summary, we computationally identified Ni_3Fe as a promising catalyst for the quinoline selective hydrogenation to 1,2,3,4-tetrahydroquinoline using density functional theory calculations and microkinetic modeling. Due to the high complexity of this reaction, we first established a Sabatier volcano for QL hydrogenation to py-THQL using the binding

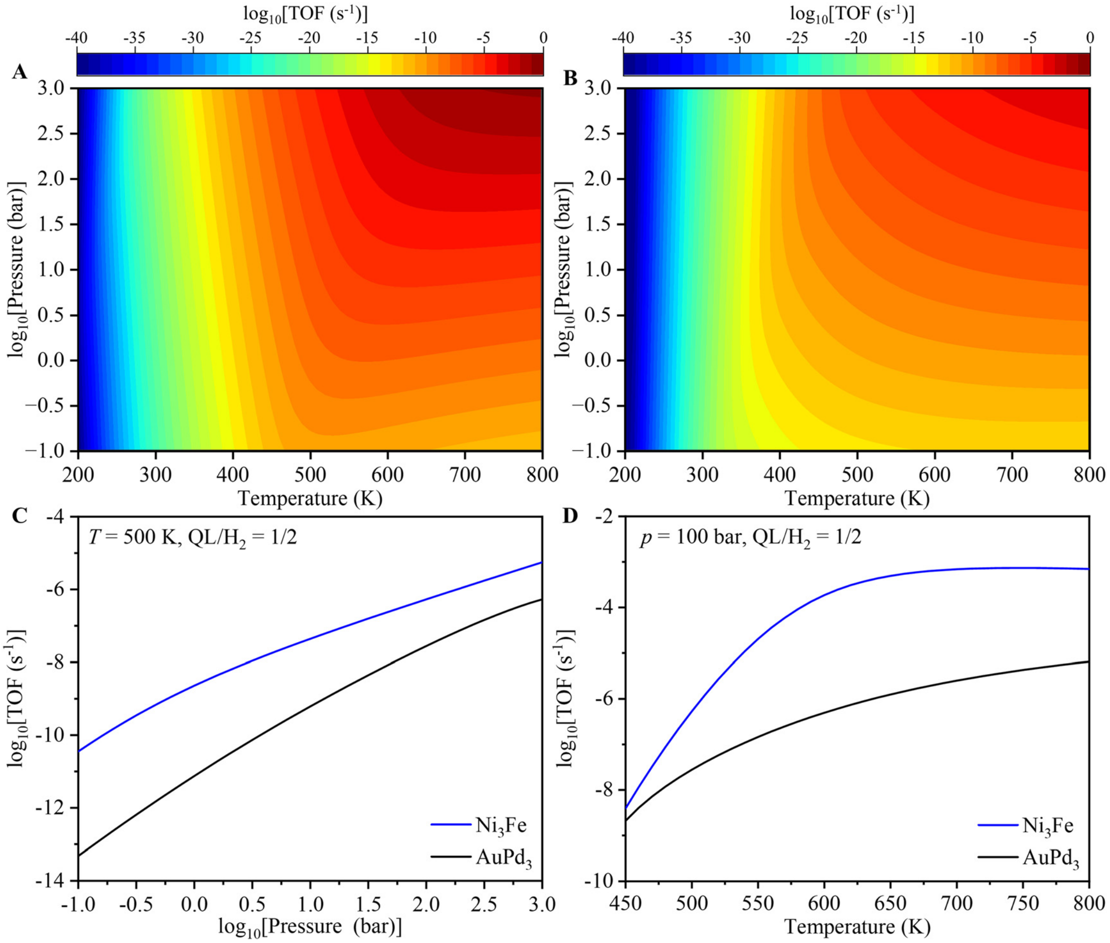

Fig. 3 Calculated TOF of py-THQL production as a function of temperature and total pressure at QL/H$_2$ = 1/2 on the Ni$_3$Fe(111) surface (A) and AuPd$_3$(111) surface (B), as well as the pressure dependence at 500 K (C) and temperature dependence at 100 bar (D) with QL/H$_2$ = 1/2.

energy of QL as an adequate descriptor. Then, a systematic evaluation of the descriptor values and stabilities on 18 bimetallic alloys composed of earth-abundant elements results in identifying Ni$_3$Fe as a good candidate with moderate binding strength of QL and high stability. Further systematic mechanism calculations on the Ni$_3$Fe(111) surface showed that the reaction favorably followed subsequent hydrogenation of the C$_1$, C$_2$, C$_3$, and N$_4$ sites on the N-heterocycle of QL, where the energy barrier for the rate-determining step was much lower than that on the AuPd$_3$(111) surface. Eventually, our MKM results also show a much higher TOF of this theoretically predicted Ni$_3$Fe than the AuPd$_3$ catalyst for py-THQL production. This work not only computationally identified an earth-abundant catalyst with high performance in QL hydrogenation but also illustrated the high capability of the Sabatier principle to guide rational catalyst design for complex reactions.

Data availability

The data supporting this article have been included as part of the ESI.†

Conflicts of interest

There are no conflicts to declare.

Acknowledgements

T. W. is thankful for the start-up packages from Westlake University and the Research Center for Industries of the Future (RCIF) at Westlake University for supporting this work. We thank the Westlake University HPC Center for computation support.

Notes and references

1 V. Sridharan, P. A. Suryavanshi and J. C. Menendez, *Chem. Rev.*, 2011, **111**, 7157–7259.

2 I. Muthukrishnan, V. Sridharan and J. C. Menendez, *Chem. Rev.*, 2019, **119**, 5057–5191.

3 Z.-Z. Wei, F.-J. Shao and J.-G. Wang, *Chin. J. Catal.*, 2019, **40**, 980–1002.

4 A. R. Katritzky, S. Rachwal and B. Rachwal, *Tetrahedron*, 1996, **52**, 15031–15070.

5 R.-K. Chen, X.-C. Yang, H.-N. Tian and L.-C. Sun, *J. Photochem. Photobiol., A*, 2007, **189**, 295–300.

6 Y. Hao, X.-C. Yang, J.-Y. Cong, A. Hagfeldt and L.-C. Sun, *Tetrahedron*, 2012, **68**, 552–558.

7 K. Rakstys, J. Solovjova, T. Malinauskas, I. Bruder, R. Send, A. Sackus, R. Sens and V. Getautis, *Dyes Pigm.*, 2014, **104**, 211–219.

8 T. Kubo, C. Katoh, K. Yamada, K. Okano, H. Tokuyama and T. Fukuyama, *Tetrahedron*, 2008, **64**, 11230–11236.

9 K. Maruoka, T. Miyazaki, M. Ando, Y. Matsumura, S. Sakane, K. Hattori and H. Yamamoto, *J. Am. Chem. Soc.*, 2002, **105**, 2831–2843.

10 R. H. Fish, A. D. Thormodsen and G. A. Cremer, *J. Am. Chem. Soc.*, 1982, **104**, 5234–5237.

11 M. Campanati, A. Vaccari and O. Piccolo, *J. Mol. Catal. A: Chem.*, 2002, **179**, 287–292.

12 J. Xia, D. Wang, R. Yang, Y. Deng and G.-J. Deng, *Green Chem.*, 2024, **26**, 5160–5166.

13 M. Wang, C. Zhang, C. Ci, H. Jiang, P. H. Dixneuf and M. Zhang, *J. Am. Chem. Soc.*, 2023, **145**, 10967–10973.

14 S. Zhang, Z.-M. Xia, T. Ni, H. Zhang, C. Wu and Y.-Q. Qu, *J. Mater. Chem. A*, 2017, **5**, 3260–3266.

15 K. Li, B.-C. Hao, M. Xiao, Y.-W. Kuang, H.-Y. Shang, J. Ma, Y. Liao and H. Mao, *Appl. Surf. Sci.*, 2019, **478**, 176–182.

16 G. Perot, *Catal. Today*, 1991, **10**, 447–472.

17 L. Tao, Q. Zhang, S.-S. Li, X. Liu, Y.-M. Liu and Y. Cao, *Adv. Synth. Catal.*, 2015, **357**, 753–760.

18 X.-F. Tu and L.-Z. Gong, *Angew. Chem., Int. Ed.*, 2012, **51**, 11346–11349.

19 S. Murahashi, Y. Imada and Y. Hirai, *Bull. Chem. Soc. Jpn.*, 1989, **62**, 2968–2976.

20 G. E. Dobereiner, A. Nova, N. D. Schley, N. Hazari, S. J. Miller, O. Eisenstein and R. H. Crabtree, *J. Am. Chem. Soc.*, 2011, **133**, 7547–7562.

21 Y.-T. Gong, P.-F. Zhang, X. Xu, Y. Li, H.-R. Li and Y. Wang, *J. Catal.*, 2013, **297**, 272–280.

22 S. Zhang, Z.-M. Xia, T. Ni, Z.-Y. Zhang, Y.-Y. Ma and Y.-Q. Qu, *J. Catal.*, 2018, **359**, 101–111.

23 M. Fang and R. A. Sánchez-Delgado, *J. Catal.*, 2014, **311**, 357–368.

24 A. Sánchez, M.-F. Fang, A. Ahmed and R. A. Sánchez-Delgado, *Appl. Catal., A*, 2014, **477**, 117–124.

25 Y. Hu, X. Li, M. Liu, S. Bartling, H. Lund, J. Rabeah, P. J. Dyson, M. Beller and R. V. Jagadeesh, *ChemCatChem*, 2024, **16**, e202301027.

26 X. Wei, Y. Jiang, Y. Ma, H. Liao, S. Dai, P. An, Z.-Q. Wang, X.-Q. Gong and Z. Hou, *ACS Catal.*, 2024, **14**, 5344–5355.

27 J.-W. Zhang, D.-D. Li, G.-P. Lu, T. Deng and C. Cai, *ChemCatChem*, 2018, **10**, 4966–4972.

28 Y.-G. Chen, Z.-J. Yu, Z. Chen, R.-G. Shen, Y. Wang, X. Cao, Q. Peng and Y.-D. Li, *Nano Res.*, 2016, **9**, 2632–2640.

29 J.-Q. Bai, M. Tamura, Y. Nakagawa and K. Tomishige, *Catal. Sci. Technol.*, 2022, **12**, 2420–2425.

30 R.-R. Yun, L.-R. Hong, W.-J. Ma, S.-N. Wang and B.-S. Zheng, *ACS Appl. Nano Mater.*, 2019, **2**, 6763–6768.

31 J.-B. Zhao, H.-F. Yuan, G. Yang, Y.-F. Liu, X.-M. Qin, Z. Chen, C. Weng-Chon, L.-M. Zhou and S.-M. Fang, *Nano Res.*, 2021, **15**, 1796–1802.

32 X.-J. Cui, Z.-J. Huang, A. P. van Muyden, Z.-F. Fei, T. Wang and P. J. Dyson, *Sci. Adv.*, 2020, **6**, eabb3831.

33 P. Zheng, C. Xiao, S. Song, A. Duan and C. Xu, *J. Hazard. Mater.*, 2021, **411**, 125127.

34 L.-F. Yin, J.-L. Ma, L.-X. Ling, R.-G. Zhang, G.-C. Yan, J.-L. Wang, W.-M. Lu, Y. Li and B.-J. Wang, *Mol. Catal.*, 2023, **538**, 112970.

35 C. J. Jacobsen, S. Dahl, B. S. Clausen, S. Bahn, A. Logadottir and J. K. Norskov, *J. Am. Chem. Soc.*, 2001, **123**, 8404–8405.

36 J. K. Nørskov, T. Bligaard, J. Rossmeisl and C. H. Christensen, *Nat. Chem.*, 2009, **1**, 37–46.

37 A. J. Medford, A. Vojvodic, J. S. Hummelshøj, J. Voss, F. Abild-Pedersen, F. Studt, T. Bligaard, A. Nilsson and J. K. Nørskov, *J. Catal.*, 2015, **328**, 36–42.

38 S.-H. Liu, N. Govindarajan and K. Chan, *ACS Catal.*, 2022, **12**, 12902–12910.

39 T. Wang, J. Ibañez, K. Wang, L. Fang, M. Sabbe, C. Michel, S. Paul, M. Pera-Titus and P. Sautet, *Nat. Catal.*, 2019, **2**, 773–779.

40 G. M. Xu, C. Cai and T. Wang, *J. Am. Chem. Soc.*, 2022, **144**, 23089–23095.

41 G. M. Xu, C. Cai, W. H. Zhao, Y. H. Liu and T. Wang, *WIREs Comput. Mol. Sci.*, 2022, **13**, e1654.

42 G. Kresse and J. Furthmüller, *Comput. Mater. Sci.*, 1996, **6**, 15–50.

43 J. Wellendorff, K. T. Lundgaard, A. Møgelhøj, V. Petzold, D. D. Landis, J. K. Nørskov, T. Bligaard and K. W. Jacobsen, *Phys. Rev. B: Condens. Matter Mater. Phys.*, 2012, **85**, 235149.

44 G. Henkelman, B. P. Uberuaga and H. Jónsson, *J. Chem. Phys.*, 2000, **113**, 9901–9904.

45 S. R. Bahn and K. W. Jacobsen, *Comput. Sci. Eng.*, 2002, **4**, 56–66.

46 P. Paufler, *Cryst. Res. Technol.*, 1987, **22**, 1436.

47 I. Chicinas, V. Pop and O. Isnard, *J. Magn. Magn. Mater.*, 2002, **242–245**, 885–887.

48 I. Chicinaș, V. Pop, O. Isnard, J. M. Le Breton and J. Juraszek, *J. Alloys Compd.*, 2003, **352**, 34–40.